PNAS RESEARCH ARTICLE | NEUROSCIENCE OPEN ACCESS

Precision proteoform design for 4R tau isoform selective templated aggregation

Andrew P. Longhini[a,b], Austin DuBose[c], Samuel Lobo[d], Vishnu Vijayan[c], Yeran Bai[a,b,e], Erica Keane Rivera[a,b], Julia Sala-Jarque[a,b], Arina Nikitina[a,b], Daniel C. Carrettiero[a,b,f], Matthew T. Unger[a,b], Olivia R. Sclafani[a,b], Valerie Fu[a,b], Emily R. Beckett[a,b], Michael Vigers[c], Luc Buée[g,h], Isabelle Landrieu[i,j], Scott Shell[d], Joan E. Shea[c,k], Songi Han[c,d,1], and Kenneth S. Kosik[a,b,1]

Edited by Byron Caughey, National Institute of Allergy and Infectious Diseases (NIH), Hamilton, MT; received November 21, 2023; accepted February 29, 2024 by Editorial Board Member Lila M. Gierasch

Prion-like spread of disease-specific tau conformers is a hallmark of all tauopathies. A 19-residue probe peptide containing a P301L mutation and spanning the R2/R3 splice junction of tau folds and stacks into seeding-competent fibrils and induces aggregation of 4R, but not 3R tau. These tau peptide fibrils propagate aggregated intracellular tau over multiple generations, have a high β-sheet content, a colocalized lipid signal, and adopt a well-defined U-shaped fold found in 4R tauopathy brain-derived fibrils. Fully atomistic replica exchange molecular dynamics (MD) simulations were used to compute the free energy landscapes of the conformational ensemble of the peptide monomers. These identified an aggregation-prohibiting β-hairpin structure and an aggregation-competent U-fold unique to 4R tauopathy fibrils. Guided by MD simulations, we identified that the N-terminal-flanking residues to PHF6, which slightly vary between 4R and 3R isoforms, modulate seeding. Strikingly, when a single amino acid switch at position 305 replaced the serine of 4R tau with a lysine from the corresponding position in the first repeat of 3R tau, the seeding induced by the 19-residue peptide was markedly reduced. Conversely, a 4R tau mimic with three repeats, prepared by replacing those amino acids in the first repeat with those amino acids uniquely present in the second repeat, recovered aggregation when exposed to the 19-residue peptide. These peptide fibrils function as partial prions to recruit naive 4R tau—ten times the length of the peptide—and serve as a critical template for 4R tauopathy propagation. These results hint at opportunities for tau isoform–specific therapeutic interventions.

tauopathies | prion-like templating | amyloidogenic core | protein misfolding

Significance

A structural motif corresponding to a short junction sequence spanning R2 and R3 forms fibrils that adopt a fold characteristic of 4R tauopathy fibrils and induces misfolding of the larger tau protein with loss of microtubule binding and a prion-like specificity for 4R tau. Simulations, validated experimentally, pinpointed the specific amino acids in the peptide that can toggle its properties between aggregation competent and incompetent. The modifications suggest design principles for a therapeutic intervention potentially capable of disaggregating tau or preventing its aggregation in the 4R tauopathies.

The pathogenetic mechanisms of tauopathies critically involve a prion-like spread of misfolded tau, often displaying disease-specific topographies and conformations (1–3). Prion-like tau protein spread can be defined as strain-specific generation and propagation of a distinct amyloid shape within the brain (4–6). As tau strains spread from cell to cell, the donor protein accurately templates the misfolding of tau in the recipient cells. Capturing tau for templating requires the prion-like donor tau to select a tau conformer from a broad energy landscape containing an ensemble of conformers that will lead to the replication of misfolded tau with the specific atomic level structures as adopted in fibrils diagnostic of the clinical phenotypes of tauopathies, such as chronic traumatic encephalopathy (CTE), frontotemporal dementias, and Alzheimer's disease (AD) (7). The exact structural and dynamic molecular details of how tau transitions to specific amyloid forms under different clinical circumstances and cellular environments are still not well understood but will be necessary to produce the specific pathological conformations in vitro. The intrinsically disordered tau population is in stable equilibrium between monomers, dimers, and trimers according to a recent study using single-molecule mass photometry. However, the native-like oligomers present at equilibrium with the monomer, in the absence of aggregation-inducing factors, are thought to be off-pathway with respect to fibrillization according to recent studies (8, 9). Instead, the relevant species may be distinct conformers that tau adopts, depending on the energy landscape of the conformational ensemble of tau monomers that promote self-association by stabilizing intermolecular contacts, leading to oligomerization (10), fibrillization, and seeding in recipient cells (11). Vigers et al. (12) demonstrated that the widely used P301L mutation dramatically alters the energy landscape of the conformational ensemble of tau monomers and, as a result, drives up the population of the aggregation-competent conformers.

Two highly studied six amino acid peptides—VQIINK in repeat domain 2 (R2) and VQIVYK in repeat domain 3 (R3)—can assemble in vitro into β-sheet-rich fibrils, but these fibrils are not seed-competent (13–15). Characteristics of these sequences known

Author contributions: A.P.L., S.L., Y.B., M.V., S.S., J.E.S., S.H., and K.S.K. designed research; A.P.L., A.D., S.L., V.V., Y.B., E.K.R., J.S.-J., D.C.C., M.T.U., O.R.S., V.F., and E.R.B. performed research; A.P.L., A.D., V.V., Y.B., L.B., and I.L. contributed new reagents/analytic tools; A.P.L., A.D., S.L., V.V., Y.B., J.S.-J., A.N., D.C.C., M.V., S.H., and K.S.K. analyzed data; and A.P.L., S.H., and K.S.K. wrote the paper.

Competing interest statement: K.S.K. consults for ADRx and Expansion Therapeutics and is a member of the Tau Consortium Board of Directors.

This article is a PNAS Direct Submission. B.C. is a guest editor invited by the Editorial Board.

[1]To whom correspondence may be addressed. Email: kosik@lifesci.ucsb.edu, songi.han@northwestern.edu.

This article contains supporting information online at https://www.pnas.org/lookup/suppl/doi:10.1073/pnas.2320456121/-/DCSupplemental.

Published April 3, 2024.

as PHF6* and PHF6, respectively, have been studied through the clearance capacity of peptide mimetics targeting these amyloidogenic motifs (16–18), through nanobodies targeting PHF6 (19), and by enhancing the function of the chaperones Hsp40, Hsp70, and Hsp90, known to bind around PHF6 (20). While these short sequences in tau are recognized as amyloidogenic in vitro, little is known about the additional molecular features that confer the property of seeding. Attempts to define a minimal seed have included tau trimers (21), individual repeat peptides (22), a seed-competent monomer (23), peptides that extend the amyloidogenic hexapeptides (12, 14, 24), a 31-amino acid peptide (residues 306 to 336) (25), and a 17-amino acid peptide (residues 295 to 311) (24), but our understanding remains incomplete, and a rational design of a tau prion with predicted strain specificity has not been demonstrated to date.

For the fold adopted by the fibrillar tau to propagate monomeric tau by templating, tau monomers must stack in-register onto fibrils for prion-like propagation. Given that every distinct tau fibril structure solved to date includes PHF6 in the fibril core, it must be included in the fibril interface and stabilize a specific fold. Vigers et al. highlight that the amyloidogenic PHF6(*) motifs must be oriented such that the backbone hydrogen-bonding moieties that form the intermolecular β-sheets are positioned along the fibril growing axis, and not occupied by intramolecular β-hairpins (12). Shape propagation by templated seeding cannot be fulfilled with standalone PHF6 or PHF6* fragments that can freely rotate unless these fragments are stably held in a specific orientation with a counterstrand when forming fibrils. The 19-residue peptide fragment at the R2/R3 junction, jR2R3 (where j strands for junction), exactly achieves that requisite with the PHF6 held in place by a counterstrand stabilized by intramolecular salt-bridge and/or hydrophobic interactions, and the backbone hydrogen-bonds oriented along the fibril growing axis. The counter strand not only stabilizes the aggregation-competent orientation for PHF6, but it also offers additional shape stability. The 3 Å cryo-EM structure of the jR2R3-P301L fibril from Vigers et al. revealed that this 19-residue peptide adopted the conformation found in 4R tauopathy fibrils at the R2/R3 splice junction, in which a minimal N-terminal segment 295 to 300, as part of the second repeat of 4R tau, stabilizes and holds in place the PHF6 segment within a U-shaped fold (PDB: 8V1N, ref. 12). The fibrils formed of jR2R3-P301L, with four peptide chains folded and packed in 2D across the fibril cross-section, are highly homogeneous, abundant, stable, and seeding competent to recruit 4R tau in vitro. However, for jR2R3-P301L fibrils to qualify as tau prions, they must misfold naive tau intracellularly, propagate aggregation in a strain or isoform-specific manner, and generate insoluble tau that maintains such activity.

This study details the design of a small tau peptide with prion-like properties, elucidating how it faithfully templates the structures of 4R tauopathies. These peptide-induced 4R tau aggregates are sarkosyl-insoluble, high molecular weight assemblies that robustly propagate to daughter cells across multiple generations and passages and contain a lipid signal localized to the aggregate. We simulated the detailed molecular dynamic interaction of a seed with a localized area of native tau and validated these predictions experimentally. Experiments revealed a mechanism that lowered the energy barrier toward 4R tau oligomerization by breaking intramolecular hydrogen bonds and exposing the amyloidogenic PHF6 region such that its hydrogen bond forming functionalities were unoccupied and available for recruiting tau monomers to the active fibril end. Importantly, these observations suggest a design principle for preventing aggregate formation. Repositioning very few of the residues that define the 4R tau as in or out of the sequence could control aggregate formation. Of particular interest was the single S305K substitution in cellular tau that prevented seeding with the otherwise 4R-specific seeding-competent peptide. This mutation that rendered cellular 4R tau as 3R tau-like at one site pinpointed a structural feature involved in templating. A search among the tau fragments known to exist in tauopathy brain tissue (25–29) for those that resemble the small probe peptide used here could reveal a more precise therapeutic target.

Results

A Small Tau Peptide Induces Tau Fibrils. Two 19-amino acid tau peptides (295 to 313) designated jR2R3 and jR2R3 P301L, that differ only by the presence of the P301L mutation in jR2R3 P301L (Fig. 1*A*), can readily form fibrils (24). jR2R3 and jR2R3 P301L span the splice junction between the second and third repeat and contain the PHF6 aggregation motif (VQIVYK) (13, 16, 19). PHF6 appears in various contexts within the recently solved full-length tau fibril structures, always adopting β-strand conformations (30–35). For tauopathies containing exclusively 4R tau (corticobasal degeneration (CBD), argyrophilic grain disease (AGD), aging-related tau astrogliopathy (ARTAG), progressive supranuclear palsy (PSP), globular glial tauopathy (GGT), GGT-PSP tauopathy (GPT)), the jR2R3 sequence folds into a strand-loop-strand motif (Fig. 1*B*) (34). In pure 3R tauopathies, such as Picks' disease (PiD), which lack residues present in jR2R3 and jR2R3 P301L, the PHF6 amyloidogenic sequence does not reside in the context of a strand-loop-strand (34). For tauopathies with mixed 3R/4R isoforms [AD, chronic traumatic encephalopathy (CTE)], the N-terminal half of the jR2R3 sequence—residues 295 to 305—is not present in the solved Cryo-EM structures (30, 31) (Fig. 1*B*), but NMR studies show that 3R and 4R tau are well mixed in AD-tau seeded fibrils, and the mixed fibrils reveal no structural differences in the rigid β-sheet core or the mobile domains (36). These structural data are important for understanding the prion-like properties of the jR2R3 peptides and suggest that templating and propagation are driven by different molecular mechanisms and structural motifs in different tauopathies.

jR2R3 P301L can fibrillize both in the presence and absence of heparin (Fig. 1 *C* and *D*). In contrast, jR2R3 could only aggregate in the presence of heparin and shaking, and even under these conditions, only some of the reactions resulted in productive fibril formation, which took more than 24 h (*SI Appendix*, Fig. S1 *A* and *B*). The aggregation of jR2R3 P301L, with and without heparin, was rapid, reaching plateaus in less than 3 h. Vigers et al. demonstrated that the U-shaped fold of jR2R3 P301L stacks as a strand-loop-strand β-sheet with a hyperlocalized hotspot around sites 300 and 301 capable of promoting in-register pinning of tau for templated aggregation (12). These aggregates displayed fibril-like morphologies with characteristic periodicity as observed by TEM (Fig. 1*C*).

Next, we tested whether jR2R3 and jR2R3 P301L fibrils could seed native jR2R3 and jR2R3 P301L monomers. All peptide seeds had excess heparin removed to prevent residual cofactor-induced fibrillization. In both cases, jR2R3 and jR2R3 P301L fibrils were able to propagate fibrils from jR2R3 and jR2R3 P301L monomers (*SI Appendix*, Fig. S1 *C* and *D*).

We tested whether jR2R3 and jR2R3 P301L fibrils could seed the larger tau constructs, Tau187-WT and Tau187-P301L (a.a. 255 to 441 includes core structures observed in cryo-EM tauopathies) (Fig. 1*A*). Fibrils formed from either of the peptides robustly seeded fibril growth (Fig. 1 *C* and *D*, *Bottom*, and *SI Appendix*, Fig. S1 *E* and *F*). Although jR2R3 initially has a significant barrier to aggregating into β-sheets, once it overcame this kinetic barrier and formed fibrils, its ability to template new tau monomers for further fibril propagation remained effective in vitro.

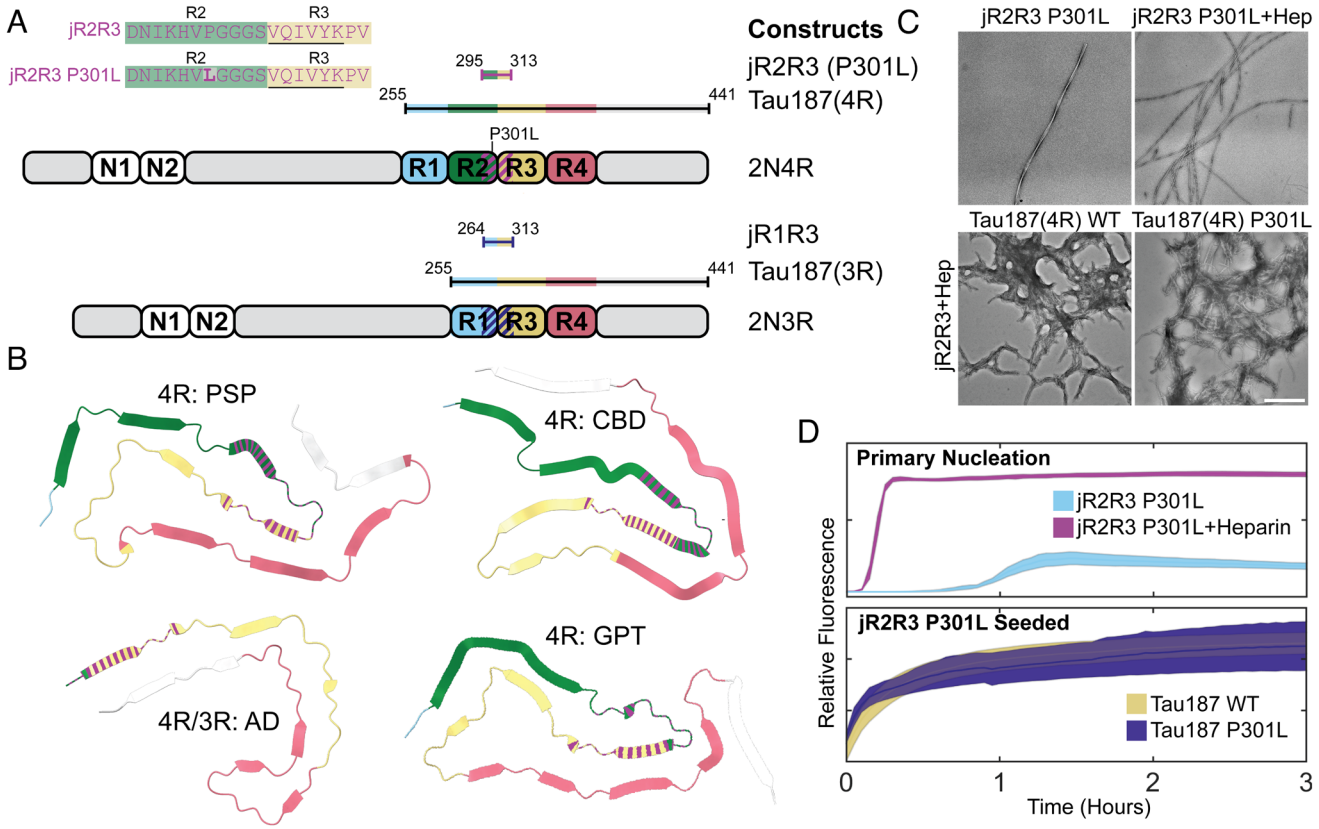

Fig. 1. Tau constructs, structural representations, and fibrillization characteristics of jR2R3 and jR2R3 P301L. (*A*) Overview of the tau constructs utilized in the study, including 3R and 4R isoforms. These strand loop strand sequences, designated jR2R3 and jR2R3 P301L, are shown in the *Top Left* with the PHF6 sequence underlined and residues mutated relative to jR2R3 shown in bold. The diagram also illustrates the most used constructs, categorizing jR2R3, jR2R3 P301L, and Tau187(4R) as 4R tau constructs, and categorizing Tau187(3R) and jR1R3 as 3R tau constructs. The elements are color-coded for clarity with R1 highlighted in Cyan, R2 in Green, R3 in Sand, R4 in Rose, and jR2R3 and jR2R3 P301L in Purple. The dashed line on 2N4R and 2N3R represents the jR2R3/jR2R3 P301L junctions. (*B*) PDB structures representing 4R tauopathies (PSP with PDB ID: 7P65 (34), CBD with PDB ID: 6VHA (31), GPT with PDB ID: 7P6A (34), and mixed 4R/3R tauopathy (AD with PDB ID: 6VHL) (32). The jR2R3 and jR2R3 P301L constructs are centrally located in 4R tauopathies and are hypothesized to be minimal elements capable of specifically templating 4R isoforms. In mixed 4R/3R and 3R tauopathies, jR2R3 and jR2R3 P301L are absent due to splicing of the R2 repeat, which would hinder templating by jR2R3 and jR2R3 P301L due to clashes with the R1 alternatively spliced sequences in 3R sequences. The structures are colored with the conventions established in (*A*), with jR2R3 and jR2R3 P301L represented by striped coloration over their respective sequences. (*C*) TEM images displaying the fibrillization of jR2R3 P301L in the absence (*Top Left*) and presence of heparin (*Top Right*), as well as seeding of jR2R3 P301L with heparin seeds. (Scale bar: 500 nm.) (*D*) (*Top*) ThT assays comparing jR2R3 P301L fibrillization alone (cyan) and with heparin (purple). (*Bottom*) ThT assays after adding jR2R3 P301L heparin-seeded fibrils to Tau187 WT (sand) and Tau187 P301L (indigo) monomers. Error bounds represent SEM.

These seeded fibrils appeared more amorphous, but periodicity and a fibrillar appearance were readily observed. These results show that these short fragments were sufficient for propagating tau fibrils that extend well beyond the core amyloidogenic sequence which directly interacts with the peptide.

Seeding and Aggregation of jR2R3 P301L Induced Tau Aggregates in Cells. We evaluated seeding in H4 cells stably expressing mClover3-Tau187-P301L, a construct that encompasses the core of all disease tau fibrils solved by cryo-EM (30–35). jR2R3 P301L fibrils seeded tau aggregates (Fig. 2 *A* and *B*, *Top*). At concentrations of 2 μM jR2R3 P301L fibrils, 30 ± 7% of cells exhibited at least one visible tau aggregate 8 h post jR2R3 P301L seeding. The experiments described next were conducted relative to this benchmark: a seeding assay displaying the most cells with puncta (Fig. 2*A*). Full-length mClover3-Tau constructs were evaluated for their aggregation tendencies in the presence of jR2R3 P301L fibrils. Both mClover3-0N4R-P301L, and mClover3-2N4R-P301L robustly formed aggregates when seeded by jR2R3 P301L (Fig. 2*B* and *SI Appendix*, Fig. S2 *A* and *B*). mClover3-Tau187-WT and mClover3-0N4R-WT showed significantly less aggregation than their corresponding P301L variant counterparts (Fig. 2*B*). Additionally, mClover3-2N4R-WT showed less aggregation than the Tau187 constructs, potentially due to the aggregation inhibitory role of the N-terminus (37) (Fig. 2*B* and *SI Appendix*, Fig. S2 *B*, *Top*). More aggregates were observed in cells with mClover3-P301L constructs than the corresponding WT lines for all constructs tested, and Tau187 lines showed more aggregates when compared to full-length tau (Fig. 2 *B*, *Bottom* and *SI Appendix*, Fig. S2 *A* and *B*). For all subsequent experiments, we have used variations of the mClover3-Tau187-P301L for this reason. The less well fibrillized jR2R3 peptides were unable to seed tau aggregation across a range of concentrations up to 5 μM fibril and tested within the first 24 h after seeding. Neither monomeric jR2R3 nor jR2R3 P301L could seed aggregates in cells at any tested concentration or time scale.

Fluorescence recovery after photobleaching (FRAP) experiments indicated that the inclusions did not undergo fluorescence recovery after bleaching. Nine separate mClover3-Tau187-P301L jR2R3 P301L seeded aggregates were completely bleached, and no recovery of fluorescence was observed over several minutes (*SI Appendix*, Fig. S3*A*). Moreover, when large aggregates were half-bleached, there was no redistribution of fluorescence from the unbleached half of the aggregate (*SI Appendix*, Fig. S3*B*). Collectively, these results indicate that the tau inclusions did not display liquid-like exchange properties with the surrounding cellular space, consistent with the expectations that these are solid or gel-like aggregates.

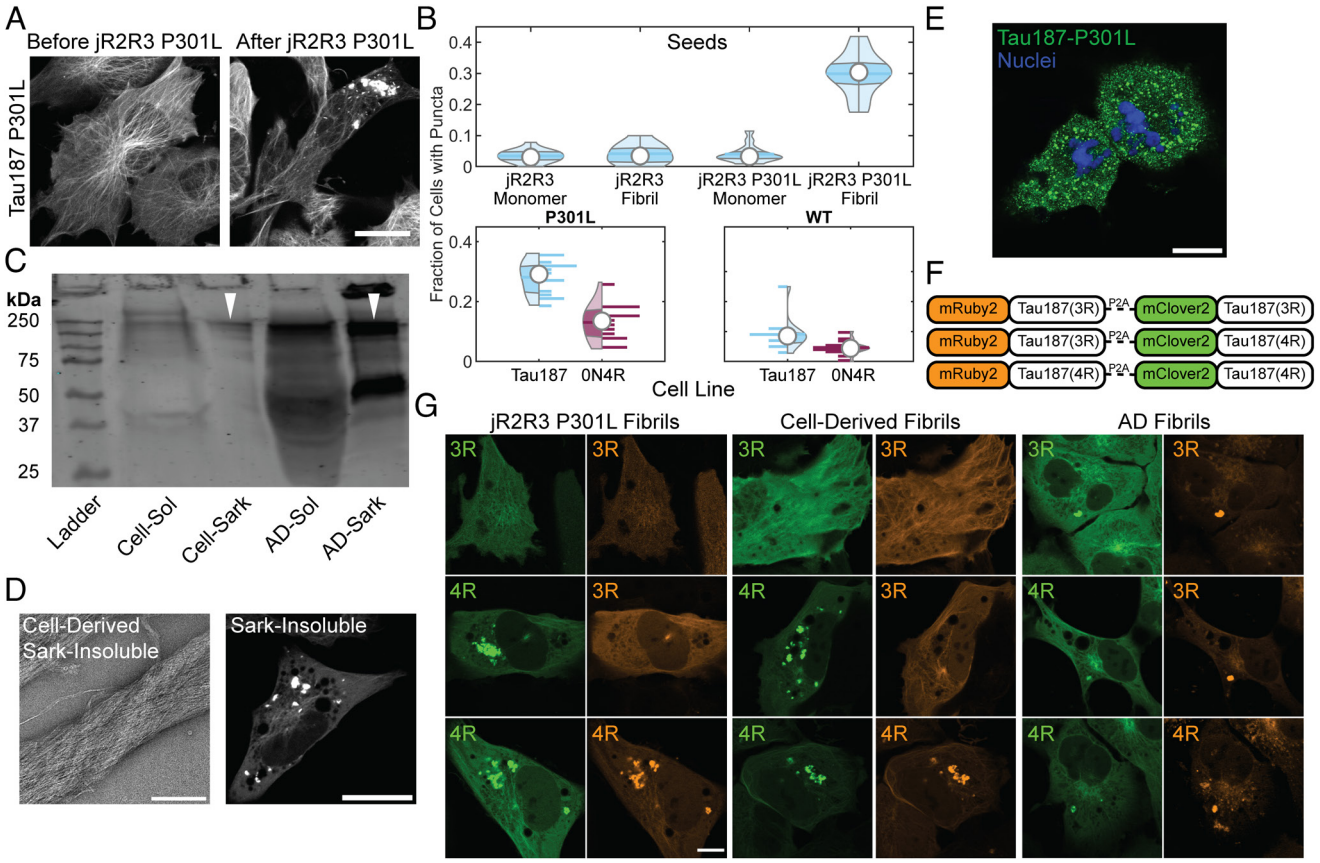

Fig. 2. Tau aggregation formation, propagation, and their characteristics in cells seeded with jR2R3 P301L fibrils. (*A*) H4 cell stably expressing mClover3-Tau187-P301L, seeded with jR2R3 P301L fibrils, imaged at 0- and 12-h post jR2R3 P301L fibril addition. (Scale bar: 20 μm.) (*B*) Violin plots of mClover2-Tau187-P301L cell lines seeded with the peptide series of monomers and fibrils (*Top*). Further analysis focused on jR2R3 P301L fibrils added to cell lines expressing Tau187 P301L or full-length 0N4R P301L (*Bottom Left*) or Tau187 WT and full-length 0N4R WT (*Bottom Right*). The percentage of cells with puncta were 5 ± 2.3% of 0N4R WT cells had puncta and 13 ± 6% of 0N4R P301L cells had puncta. Tau187 lines had the most puncta with Tau187 WT having 9 ± 5.5% and Tau187 P301L having 28 ± 5%. (*C*) Western blot of sarkosyl soluble and insoluble material from mClover3-Tau187-P301L cells seeded with jR2R3 P301L and material derived from AD brain samples. Blot stained with the disease-specific conformational tau antibody (MC1). Similar-sized oligomers observed for both cell-derived and patient-derived material highlighted with white triangles. (*D*) (*Left*) TEM of sarkosyl insoluble material derived from cell lines. (Scale bar: 250 nm.) (*Right*) Sarkosyl insoluble fractions were added to the original mClover3-Tau187-P301L cell lines showing seeding of puncta after 12 h. (Scale bar: 20 μm.) (*E*) Cells seeded with jR2R3 P301L undergo division and propagate aggregates to daughter cells. Green: Tau187-P301L, Blue: Hoechst. (Scale bar: 20 μm.) (*F*) Schematic of the three constructs used for evaluating the selective templating of either the 4R or 3R isoform of tau by jR2R3 P301L. Each construct consists of either the 4R or 3R isoform of tau fused to mRuby3 and is expressed concurrently with another 4R or 3R isoform of tau fused to mClover3. A P2A cleavage site between the two tau fusions ensures equimolar expression of the two fusions from the same expression cassette. (*G*) 12 h after the addition of jR2R3 P301L, cells expressing two copies of 4R tau showed aggregates in both channels (*Left Bottom*), cells expressing both 4R and 3R isoforms showed aggregates exclusively in the 4R channel (*Left Middle*), whereas cells expressing two copies of 3R tau exhibited no aggregates (*Left Top*). This provides strong evidence that isoform-specific templated elongation is the primary mode of propagation in these cell lines. As a control, fibrils from AD samples, which are characteristic of a mixed 4R/3R tauopathy, seeded both 3R and 4R isoforms as anticipated (*Middle*). Additionally, cell-derived material was reintroduced to the described cell lines, and selective 4R seeding was again observed (*Right*). (Scale bar: 20 μm.)

Extraction and Passaging of Cell Culture Seeded Material. Large quantities of cells expressing mClover3-Tau187-P301L were seeded with jR2R3 P301L fibrils, from which we extracted sarkosyl soluble and insoluble material. Western blots of the soluble material revealed multiple bands labeled with MC1 at ~240 kDa which would correspond to ~6-mers of mClover3-Tau187. We then compared these patterns to those from sarkosyl soluble and insoluble fractions of tau extracted from Alzheimer brain samples. MC1 positive oligomer bands ran at molecular weights that approximated 6-mers of full-length tau (Fig. 2*C*). Additionally, a fraction of the insoluble material ran at extremely high molecular weights that did not enter the wells. TEM images of the insoluble material extracted from seeded cells exhibited distinct fibril-like structures (Fig. 2 *D*, *Left*). Next, the insoluble material from the cell culture lines was added back to cells expressing mClover3-Tau187-P301L to test its seeding efficacy. The fibril fractions robustly seeded tau aggregation, whereas the soluble fractions did not (Fig. 2 *D*, *Right*).

Encouraged by the strain propagation observed with cell-extracted seeding, we cultured jR2R3 P301L seeded cells for extended periods to look for the propagation of aggregates in dividing cells. Cell lines harboring aggregates induced by jR2R3 P301L were passaged at low densities, and their division was monitored. Cells with aggregates underwent cell division, and the resulting daughter cells continued to have aggregates, suggesting authentic propagation of a strain (Fig. 2*E*). By passaging single cells into wells, we could clonally isolate cell lines that propagated the strain specifically over multiple passages.

Demonstrating 4R Selectivity of jR2R3 P301L Seeding in Cell Culture. If jR2R3 P301L is functioning as a prion-like moiety, we should be able to detect precise templating and propagation of a strain. In 4R tauopathies, 4R is selectively incorporated into fibrils (25, 37) and the fibril structure corresponds to the specific 4R tauopathy, which spreads with high structural fidelity. Considering the complementarity of the jR2R3 and jR2R3 P301L sequences

with 4R tau but not 3R tau, along with the cryo-EM structure of jR2R3 P301L fibrils that adopt a core 4R tauopathy fold (25), we hypothesized that jR2R3 P301L should be able to elongate only 4R tau isoforms. To examine selective 4R aggregate formation, we created three cell lines expressing equimolar ratios of 3R and 4R isoforms of Tau187. The two tau constructs, each labeled with a distinct fluorophore (mRuby3 or mClover3), were separated by the self-cleavable P2A sequence. This allowed for visualization isoform-selective incorporation into aggregates (Fig. 2*F*).

As anticipated, when jR2R3 P301L fibrils were introduced into cells expressing two 4R isoforms of Tau187, aggregates were observed in both channels (Fig. 2 *G*, *Left Bottom*). In contrast, cells expressing two copies of the 3R isoform of Tau187 showed no formation of aggregates (Fig. 2 *G*, *Left Top*). Finally, cells expressing one copy each of 4R and 3R Tau187 only displayed aggregates in the channel corresponding to 4R Tau187 (Fig. 2 *G*, *Left Middle*). The cell-derived material, sarkosyl extraction of insoluble Tau187 aggregates (after seeding with jR2R3 P301L fibril) was then added to dual expressing 3R/4R Tau187 cell lines (Fig. 2 *G*, *Middle*). The same selective seeding of 4R tau, as seen with jR2R3 P301L, was again observed. This outcome demonstrated the 4R selectivity of seeding. In comparison, seeding with AD brain-derived material, induced the formation of aggregates that exhibited fluorescence in both channels in each cell line, consistent with the mixed 3R and 4R tau isoform composition of AD brain fibrils (Fig. 2 *G*, *Right*) (38).

Defining the Energy Barrier to 4R Tau Fibrillization. The observation that jR2R3 P301L could seed Tau187(4R) over Tau187(3R) led us to search for unique features of the R2–R3 junction found in 4R isoforms compared to the R1–R3 junction found in 3R isoforms. Another 19 amino acid peptide that spans the R1–R3 junction is referred to as jR1R3 (Fig. 3*A*). Notably, jR2R3 and jR1R3 differ by only four amino acids while the amyloidogenic PHF6 region is shared in both sequences. We synthesized a peptide corresponding to the jR1R3 sequence and observed that, in contrast to the jR2R3 and jR2R3 P301L peptides, jR1R3 could neither fibrillize on its own, nor in the presence of heparin. None of the conditions tested, including rapid agitation, induced aggregation over any of the timescales tested despite having the amyloidogenic PHF6 sequence. We next added jR2R3 or jR2R3 P301L fibrils to jR1R3 monomers to seed jR1R3 aggregation. Again, no aggregation was observed under any condition. Thus, the four amino acid differences between these two peptides conferred strong resistance to fibrillization.

We turned to replica exchange molecular dynamics simulations (REMD), a widely used method that enhances conformational sampling of proteins by overcoming otherwise inescapable energy barriers and thus exploring extensive free energy landscapes. We observed uniform dwell times and high exchange probabilities across all temperatures sampled, demonstrating efficient temperature mixing and exploration (*SI Appendix*, Fig. S4). How might jR1R3 avoid aggregation? A clustering analysis of the replica exchange simulations of jR2R3, jR2R3 P301L, and jR1R3 identified Cluster 1 and Cluster 2 as containing the most prevalent conformations, and is described in supplementary methods (Fig. 3*B*). In our molecular dynamic simulations, we have observed two distinct types of backbone H-bonds in both Cluster 1 and Cluster 2 that help stabilize a β-hairpin conformation, specifically with the GGG motif at the turn. For ease of discussion, we have termed the H-bond nearer the GGG turn motif as the "pinch." This pinch appears to keep the hairpin structure closely bound. On the other hand, the H-bond situated closer to the ends of the molecule, which prevents them from unraveling, is termed the "clamp." Cluster 1 has an H-bond pinch between V/Q300 and S/K305 and an H-bond clamp between K298 and Q307; Cluster 2 has a H-bond pinch between V/Q300 and Q307 and a H-bond clamp between K298 and V309. These H-bonds maintain the hairpin shape in a manner that occludes the amyloidogenic PHF6 sequence.

We quantified the hairpin unfolding free energy landscapes from the replica exchange simulations of jR2R3, jR2R3 P301L, and jR1R3 as a function of the two pairs of diagnostic pinch and clamp α-carbon distances (Fig. 3*C*). In these landscapes, blue represents low energy, highly populated states, while red represents higher energy, lowly populated states. The most populated conformation (Cluster 1) is in the bottom left of the jR1R3 landscape, while Cluster 2 is slightly above it (both represented with dotted lines), and both have large energy barriers surrounding them. The landscape features distinct minima at short distances indicative of stable conformations. Interestingly, jR1R3 has a significantly larger free energy barrier to unfold than jR2R3 or jR2R3 P301L, and jR1R3 lacks a clear pathway to escape the intramolecularly H-bonded Cluster 1 and Cluster 2. The higher escape energy of jR1R3 may prevent its fibrillization, even in the presence of heparin, by protecting the amyloidogenic PHF6 sequence. This observation is consistent with the requirement for filaments to form, the intramolecular backbone H-bonds of the β-hairpin must be replaced with intermolecular backbone H-bonds as occurs in the disease state (*SI Appendix*, Fig. S5*A*, see orange dashes).

The greater tendency of jR2R3, jR2R3 P301L compared to jR1R3 to form intermolecular H-bond formation, was demonstrated by REMD simulations of dimers. jR1R3 formed significantly fewer intermolecular H-bonds compared to jR2R3 and jR2R3 P301L (*SI Appendix*, Fig. S5*B*). Specifically, conformations with five or more intermolecular H-bonds are rare when either of the monomers exhibits the H-bond pattern of Cluster 1 or Cluster 2. Based on this observation, we conclude that the intramolecularly H-bonded structures of jR1R3, jR2R3, and jR2R3 P301L in Cluster 1 and Cluster 2 conferred resistance to aggregation.

These simulations suggested that an extensive intramolecular H-bond network can safeguard 3R tau containing the junction sequence jR1R3 from aggregation in 4R tauopathies. While similar H-bonds might exist in the jR2R3 region, these are far less stable and have lower energy barriers, facilitating transitions to fibril-competent conformations. We performed the in silico mutation series of each of the four amino acid differences that converted jR1R3 to jR2R3 in a stepwise manner. Simulating these fragments with explicit-water REMD to observe differences in H-bonding, electrostatic interactions, and hydrophobic interactions revealed that each successive mutation of jR1R3 weakened the protective H-bonding network, as measured by the populations of Cluster 1 and Cluster 2 (Fig. 3*D*). Each of the four residues that differ between jR1R3 and jR2R3 modulated the extent of intramolecular hydrogen bonding and consequently protects PHF6 from aggregation more effectively in jR1R3 than jR2R3. Thus, the gradual weakening of the H-bonds made the peptide more prone to forming intermolecular H-bonds and ultimately aggregation.

The next experiment reversed the direction by mutagenizing jR2R3 to more closely resemble jR1R3 (Fig. 3*A*). Remarkably, in this case, a single mutation in jR2R3-to-jR2R3 S305K (a K in jR1R3 occurs in this position rather than an S) drastically increased the free energy barrier to monomer unfolding (Fig. 3*C*, jR2R3 S305K), increased intramolecular H-bonding, and would be predicted to prevent tau aggregation. By simulating the fragments jR2R3 and jR2R3 S305K with REMD, we observed that the S305K mutation approximately doubled the population of the aggregation-resistant Cluster 1 (Fig. 3*D*). K305's hydrophilic side

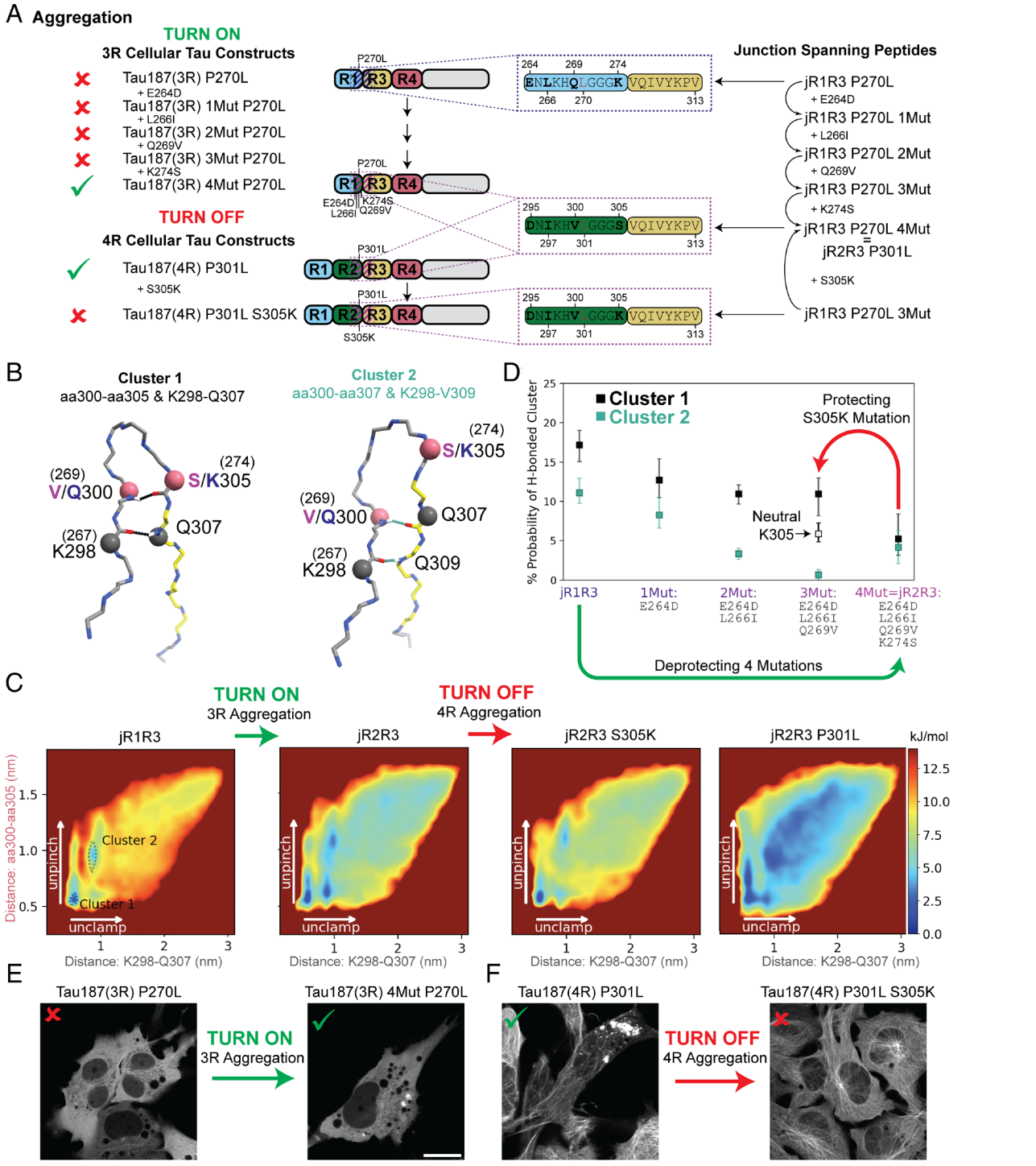

Fig. 3. Comparative analysis of energy landscapes and hydrogen bonding in jR2R3, jR2R3 P301L, and jR1R3 monomers and dimers. (*A*) Schematics illustrating the relationships between the junction-spanning peptides used in the simulations and the Tau187 constructs used in the cellular seeding assays. On the right, junction spanning peptides representing the residues 295(264)-313 in the 2N4R numbering scheme are shown. These regions are highlighted with dotted boxes in the Tau187 constructs used in the study (indigo for jR1R3 and purple for jR2R3). For each corresponding Tau187 construct, a red x or a green check mark annotates if jR2R3 P301L was able to induce puncta in the respective cell line. For 3R constructs, the P270L mutation corresponds to the P301L mutation seen in 4R isoforms. (*B*) Illustration of two most populated clusters from REMD simulations. Cluster 1 (*Top*, Black) highlights hydrogen bonds between aa300-aa305 and K298-Q307. Cluster 2 (*Bottom*, Cyan) highlights hydrogen bonds between aa300-aa307 and K298-V309. For residues with different numbering in 3R and 4R isoforms, the alternate numbering is shown in parenthesis. Rose-colored balls and black-colored balls represent the four residues that are used to construct the energy landscapes in (*C*). (*C*) Energy landscapes of α-carbon distances K298-Q307 and aa300-aa305 for (from left to right) jR1R3, jR2R3 (jR2R3 = jR1R3 4Mut), jR1R3 3Mut, and jR2R3 P301L. The y-axis represents the distance between aa300-aa305 (rose), while the x-axis represents the distance between K298-Q307 (black) and is colored as in (*B*). Clusters 1 and 2 from (*B*) are annotated in the leftmost panel (jR1R3) as dotted lines. Mutations that transition the jR1R3 peptide to the jR2R3 peptide diminish the energy wells stabilizing the hydrogen bonding in Clusters 1 and 2 (Green arrow). This effectively turns on 3R aggregation. The mutation S305K in the jR2R3 construct reestablishes the barriers and turns off 4R aggregation (Red arrow). (*D*) Monitoring the formation of two pairs of hydrogen bonds as jR2R3 transitions into jR1R3 through sequential amino acid swaps. Cluster 1 is represented by black boxes and Cluster 2 is represented with cyan boxes. Cluster 1 with a neutral K305 is shown as an unfilled black box. The bars represent 67% CI. Protecting (Red) and deprotecting (Green) mutations are highlighted as arrows and represent the mutations shown in panels (*C*, *E*, and *F*). (*E*) jR2R3 P301L added to cell lines expressing Tau187(3R) P270L did not form aggregates (*Left*), but when added to cells expressing Tau187(3R) 4mut P270L formed aggregates (*Right*). (*F*) jR2R3 P301L added to cell lines expressing Tau187(4R) P301L formed aggregates (*Left*), but when added to cells expressing Tau187(4R) S305K P301L no aggregates were observed (*Right*).

chain amine tends to orient outward to the solvent, which orients its backbone carbonyl inward where it can form an H-bond with residue 300. We simulated a deprotonated lysine and saw that the doubling of the Cluster 1 population was undone Fig. 3*D*), thus supporting our hypothesis that the charge facilitates the correct orientation of the K305 H-bond.

Experiments Validate of 4R Energy Barrier Simulations. To validate these computations, a series of 3R tau constructs, with the four sequential mutations within the 1R-3R junction to match those found in the 2R-3R junction of Tau187-P301L, were introduced (Fig. 3 *A*, *Left*). In essence, we made a 3R Tau187-P301L that replaced four amino acids of the first repeat with those of the second repeat resulting in a 3R tau that resembled a 4R tau. These constructs were labeled mClover3-Tau187(3R)-P270L to indicate the corresponding site in the 1R-3R sequence with the Tau187-P301L mutation in the second repeat. The mutations were mClover-Tau187(3R)-P270L-E264D, mClover3-Tau187(3R)-P270L-E264D-L266I,mClover3-Tau187(3R)-P270L-E264D-L266I-Q269V, and mClover3-Tau187(3R)-P270L-E264D-L266I-Q269V-K274S. We introduced jR2R3 P301L fibrils to cell lines stably expressing each construct and aggregates were only observed in the construct with all four mutations, i.e., the Tau187(3R) constructs with the jR1R3 segment mutated to mimic the jR2R3 segment (Fig. 3*E*). In other words, a 3R-like tau could be made to aggregate like 4R tau by mutations targeting only the short jR2R3 region. This outcome validates our simulations and suggests that the local structure around the exposed PHF6 motif plays a crucial role in isoform-selective seeded aggregation. Thus, jR2R3 P301L–induced fibrils rely on a specific set of residues to enable seeding of 4R tau due to exposure of the PHF6 sequence.

While these 4R mutations altered the resistance of 3R tau to aggregate so that it became competent to be recruited to jR2R3 P301L 4R–specific tau aggregation, the next question was whether we could prevent 4R aggregation by introducing a mutation into the second repeat that made its structure more similar to 3R tau, and hence resistant to the induction of jR2R3 P301L-induced tau aggregation. In position 305, immediately amino to the VQIVYK amyloidogenic sequence, a serine is present in the R2–R3 junction, and a lysine is present in the R1–R3 junction. Remarkably, when jR2R3 P301L fibril seed was introduced to a cell line expressing Tau187-P301L-S305K, no significant aggregation was seen (Fig. 3*F*) consistent with the predictions from the REMD simulations. As expected, neither Tau187(3R) nor Tau187(3R)-P270L mutant could be seeded by jR2R3 P301L fibrils in any of our cell culture experiments. This experiment suggests that the single S305K mutation could serve as a prevention of 4R tauopathies.

Binding of Z70 Nanobody Inhibits Peptide-Induced Seeding. We used the previously described camelid heavy-chain-only antibody VHH Z70 (19) with a binding sequence that is coextensive with the PHF6 sequence. VHH Z70 forms five intermolecular hydrogen bonds between VHH Z70 and PHF6. The PHF6 sequence, derived from the structure of disease fibrils, aligns with the crystallized VHH Z70 bound to a free PHF6 peptide (Fig. 4 *A* and *B*) (30). Cell lines stably expressing mClover3-Tau187-P301L were transiently transfected with VHH Z70-mCherry and subsequently exposed to jR2R3 P301L fibrils. Twelve hours later,

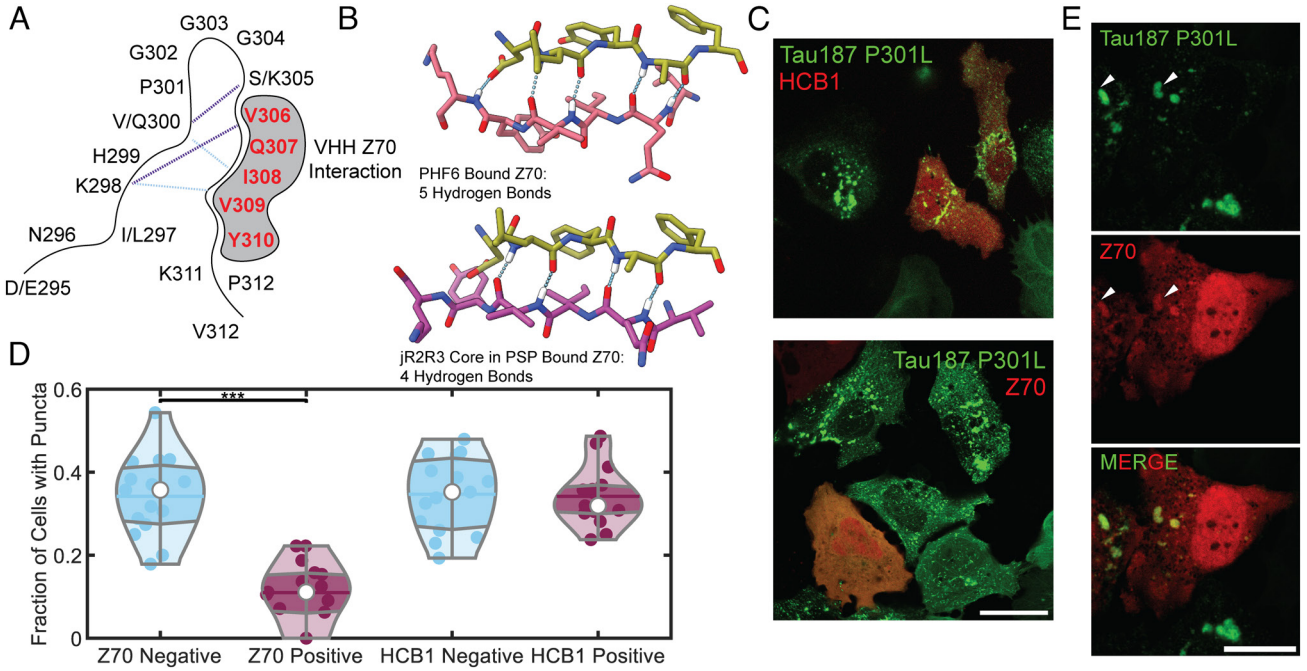

Fig. 4. Investigation of the effect of VHH Z70 nanobody on jR2R3 P301L-induced tau fibrillization in cells. (*A*) Schematic representation of the SLS hairpin and its most populated hydrogen bonds as determined with molecular dynamics (Cluster 1 in purple and Cluster 2 in cyan dashed lines). The interaction with ZHH Z70 is highlighted by gray shading and its interaction site, the PHF6 motif is represented in red. (*B*) The crystal structure [PDB:7QCQ (19)] of VHH Z70 in olive bound to PHF6 in rose reveals five hydrogen-bond contacts between the molecules (*Left*). An alignment of the PHF6 sequence from the PSP fibril [PDB:7P65 (32), purple, *Right*] with that bound in the crystal structure of VHH Z70 shows an RMSD 0.848, with four potential hydrogen bond contacts, suggesting that the VHH Z70 nanobody could recognize 4R tauopathy fibrils. (*C*) jR2R3 P301L sonicated fibrils were introduced to stable H4 cell lines expressing mClover3-Tau187-P301L, with a subset of cells transiently expressing a nanobody-mCherry fusion against Huntingtin protein (HCB1) or PHF6 (VHH Z70) in red. Notably, cells expressing VHH Z70 generated fibrils less frequently than those that did not express VHH Z70. (Scale bar: 30 μm.) (*D*) Quantification of the data from (*C*) indicates that cells with VHH Z70 formed puncta 11 ± 7% of the time, whereas those without VHH Z70 exhibited puncta in 34 ± 10% of cells, suggesting an inhibitory effect of VHH Z70 on fibril formation. HCB1 expression had no effect of fibril formation with cells expressing HCB1 having puncta in 32 ± 8% and cells without HCB1 expression forming puncta 34 ± 9% of the time. (*E*) Upon addition to preformed aggregates, the VHH Z70 nanobody exhibited clear colocalization with a subset of the tau aggregates, as indicated by white arrowheads. (Scale bar: 20 μm.)

cells were imaged. Analysis in both the mClover-Tau187-P301L and mCherry-VHH Z70 nanobody channels revealed that cells expressing the camelid nanobody contained significantly fewer aggregates, compared to cells lacking mCherry-VHH Z70 (11 ± 7% vs. 34 ± 10% of cells, $P = 2.3 \times 10^{-8}$, Fig. 4 *C* and *D*). As a control, a nanobody targeting the huntingtin protein, HCB1, showed no difference in puncta formation (32 ± 8% vs. 34 ± 9%) (39). These results suggest that VHH Z70 can inhibit jR2R3 P301L-seeded aggregation of Tau187-P301L, similar to the seeding experiment using microtubule binding region tau peptide fibrils in HEK293T biosensor lines (19). This, again, confirms that the jR2R3 P301L fibrils serve as mini-4R-tauopathy-specific seeds by directly interacting with the PHF6 region.

We next preformed cellular aggregates by exposing cells to jR2R3 P301L fibrils first and subsequently transfected cells with mCherry-VHH Z70 in an attempt to clear established aggregates. Under these conditions, there was considerable cell death and therefore it was not possible to determine whether aggregates were cleared. However, there were sufficient cells to clearly observe colocalization of the nanobody signal with aggregates (Fig. 4*E*) and demonstrated that the nanobody recognized the aggregated tau populations.

jR2R3 P301L-Seeding Induces Global Structural Modifications. The variety of cellular studies presented so far showed that the jR2R3 P301L fibrils serve as mini-4R-tauopathy prions that effectively seed naive Tau187, 0N4R tau, and 2N4R tau constructs that are 10 to 20 times the length of the jR2R3 P301L fragment. These observations establish that indeed the jR2R3 region is the critical contact point for templated 4R aggregation. The question is then whether a large portion of the tau protein is ordered and incorporated into fibrils when recruited by the jR2R3 P301L seed. To answer this question, we sought to measure the distance changes across tau in the region outside the jR2R3 segment. For this, the seeded material was analyzed by double electron–electron resonance (DEER) experiments to probe the intramolecular fold of tau within the fibrillar aggregates. The distances selected for DEER measurements in Fig. 5*A* were intentionally chosen to showcase regions of Tau187 that are far removed from the immediate vicinity of the jR2R3 P301L peptide and demonstrate the long-range conformational influence exerted by the small peptide, emphasizing its far-reaching templating effects on tau's structure. A pair of spins were attached to tau at two cysteine residues, with one pair spanning sites 334 to 360 and another across sites 351 to 373. The distribution of distances measured between these probes reflects the range of ensemble conformations sampled by the protein. To avoid measuring intermolecular distances, doubly spin-labeled tau is mixed with WT tau at a 1:10 ratio. The results then represent a probability density of intramolecular distances across the select pair of spin labels. The specific site pairs that were selected to inform us about the tertiary fold adopted by the seeded tau constructs, e.g., to differentiate between AD, CBD, PSP, and GPT fibrils.

The structures formed from jR2R3 P301L fiber-seeded Tau187(4R) material differed substantially from heparin-seeded fibrils (Fig. 5 *A* and *B*). Specifically, pairwise distribution plots showed broad distributions for heparin fibrils for both the 334 to 360 distance (*SI Appendix*, Fig. S5*A*) and the 351 to 373 distance (Fig. 5*A*). This indicates a sampling of many conformations of fibrils as predicted from the cryo-EM structures of heparin-seeded tau (33). In contrast, jR2R3 P301L-seeded Tau187 fibrils, displayed a narrower distance distribution, indicating a smaller sampled space compared to heparin-seeded fibrils. Interestingly, the 351 to 373 distance pair, which is predicted to sample widely different distances in PSP, GPT, and CBD fibrils, demonstrated a substantial compaction of the P(R) curve centered at 2.5 nm (Fig. 5*A*). This corresponds to the distance between these two residues in the GPT and PSP cryo-EM structures (34). Unlike the broader peaks observed for both Tau187 monomer and heparin-induced Tau187 fibrils, the peak resulting from the jR2R3 P301L seeded sample is notably narrower and consists of a single, distinct peak, rather than a composite of multiple peaks. Biological triplicate measurements confirmed this observation. Unlike the 351 to 373 probe pair, the 334 to 360 probe pair yielded multiple distance peaks that did not correspond closely to PSP, GPT, or the

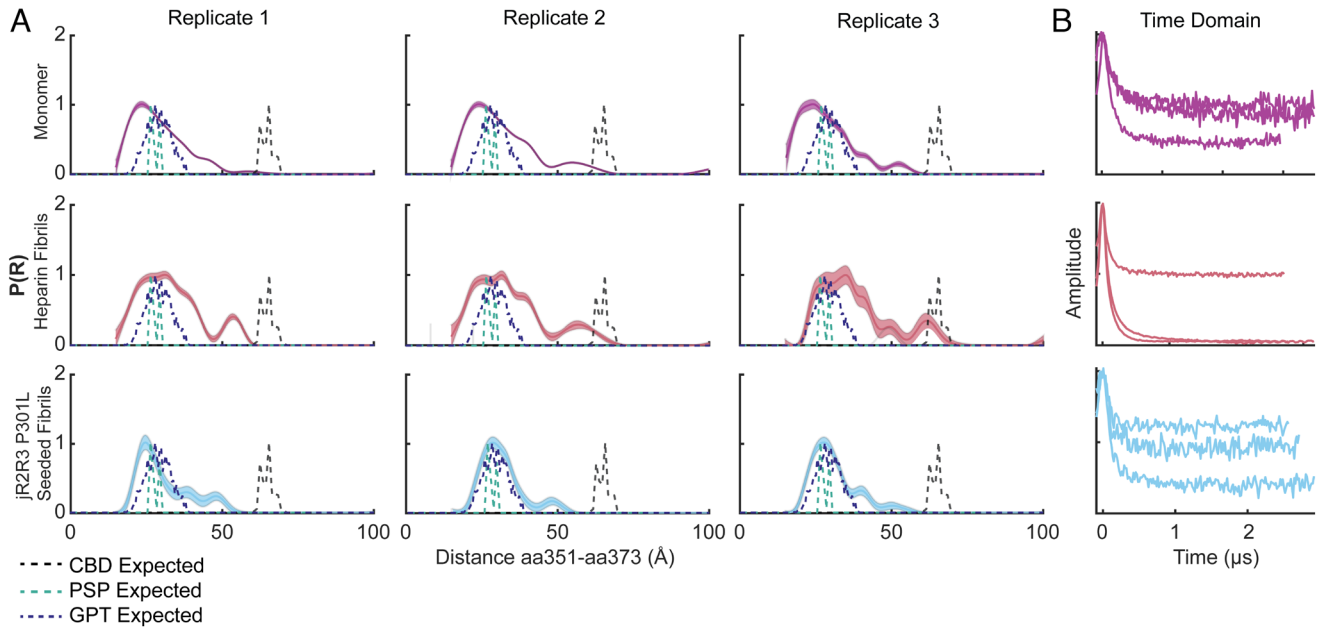

Fig. 5. Comparative analysis of DEER measurements for monomeric and fibrillar tau configurations. (*A*) DEER distance distribution plots (P(R)) for the 351 to 373 spin-pair distances in various tau configurations. The monomer is represented in purple, jR2R3 P301L seeded fibril in cyan, heparin fibril in rose, while the predicted distances for CBD are in black, PSP are in teal, and GPT are in indigo. Triplicates of each condition are plotted across the columns. (*B*) The time domain data for each of the replicates plotted in (*A*).

CBD distances (*SI Appendix*, Fig. S6 *A*, *B*, *D*, and *E*). Instead, they revealed a heterogeneous distance probability distribution that is likely indicative of greater disorder across this distance. Nevertheless, the peaks sampled differed from the heparin-induced distance pair and were narrower and distinct from monomer data. This narrowing of the peaks induced by jR2R3 P301L reinforces the idea that the seed guides Tau187 to a less heterogenous set of structures. Taken together, these data, aligned with cryo-EM structure of jR2R3 P301L fibrils that most closely resembles the GPT distances, suggest that this peptide is capable of templating discrete large structural changes throughout the tau protein and partially captures the GPT distance, a hybrid structure between that in CBD and PSP.

jR2R3 P301L-Seeded Aggregates have Cross-β-Strand Structure and an Associated Lipid Signal by Optical Photothermal Infrared Microscopy. Optical photothermal infrared (O-PTIR) microscopy, which provides submicrometer resolution infrared imaging (40–43) was used to probe the structure of jR2R3 P301L-seeded cellular aggregates. In O-PTIR, each pixel of the microscopic image contains an IR spectrum over a defined range of wavenumbers allowing for the investigation of the chemical and structural composition at specific fluorescent structures (Fig. 6 *A* and *B*). Measurements of the cellular aggregates revealed a significantly higher cross-β-strand content compared to the cytoplasm, as indicated by the substantial difference in the mean values of the ratio of peaks at 1,634 cm^{-1} and 1,654 cm^{-1} ($P = 1.6 \times 10^{-5}$, Fig. 6*D*). This result is consistent with the expected properties of aggregates forming fibril-like structures. Interestingly, a local increase in signal at 1,750 cm^{-1} associated with the aggregate was observed, indicative of a lipid signal. When compared to the cytoplasm, the difference in the ratios of 1,750 cm^{-1} and 1,654 cm^{-1} was also highly significant ($P = 7.8 \times 10^{-7}$, Fig. 6*D*).

To probe the autophagy pathway and elucidate the lipid signal's nature, we assessed tau aggregates' colocalization with lysosomal marker Lamp1 and autophagosomal marker LC3 in jR2R3 P301L-seeded cells (Fig. 6*C* and *SI Appendix*, Fig. S7*A*). This analysis revealed minimal overlap with Lamp1 and a modest association with LC3, particularly with larger tau aggregates. In contrast, pronounced colocalization with SQSTM1 and VCP suggests alternative degradation mechanisms, such as aggresomes, may be involved in clearing large tau inclusions (*SI Appendix*, Fig. S7 *B* and *C*) (44–55). Systematic observation of tau aggregation over 10 h revealed diverse morphologies and a biexponential distribution in the total area and number of aggregates per cell, with dynamic growth and shrinkage in aggregate size and number, highlighting complex aggregation behaviors (*SI Appendix*, Fig. S8) (56). A more nuanced discussion of the aggregate behavior is included in *SI Appendix*, *SI Text*.

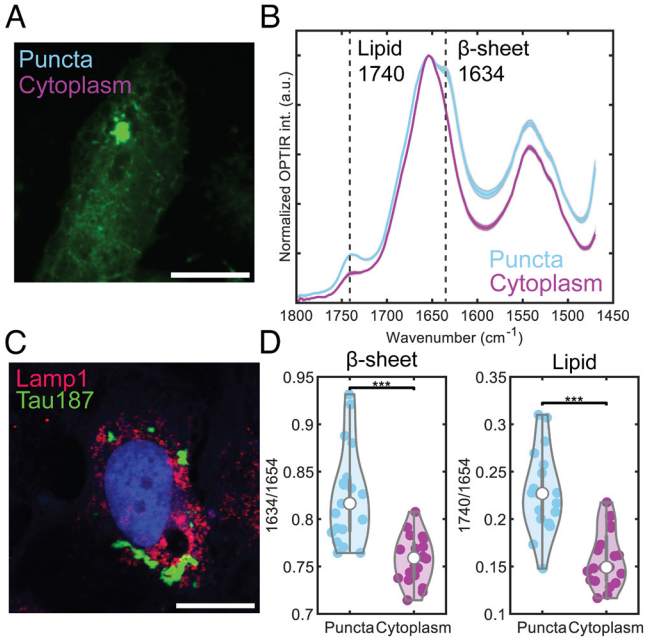

Fig. 6. Presence of lipid in jR2R3 P301L-seeded cellular aggregates using optical photothermal infrared microscopy and analysis of lysosomal markers. (*A*) O-PTIR interrogation of cells expressing mClover3-Tau187-P301L. Measurements (depicted as cyan and purple dots) were taken on tau aggregates and cytoplasm, respectively. (Scale bar: 15 μm.) (*B*) Averaged spectra of measurements from (*A*), with distinct peaks at 1,740 cm^{-1} (lipid) and 1,634 cm^{-1} (β-sheet) in aggregates. Error bars represent SEM. (*C*) Representative cell stained with Lamp1 antibody (red) to visualize lysosomes. Tau187 puncta signal (green) shows minimal colocalize with Lamp1 signal. (Scale bar: 20 μm.) (*D*) Quantification of lipid and β–sheet content from 20 independent measurements in aggregates (cyan) and cytoplasm (purple), for both lipid and B-sheet in aggregates revealing highly significant differences.

Discussion

PHF6 and PHF6* oligomers, rich in β-strand content (13), can form self-complementary beta-sheet pairs known as steric zippers (57), but they are unable to template tau misfolding in cells. By extending the PHF6(*) core to include portions of the tau repeat 2 and 3 sequences, seeding active fibrils can be generated (18, 22, 58, 59). However, a higher-order structural motif is needed to orient and hold the PHF6 segment with its hydrogen bond forming backbone moieties oriented along the fibril axis and to achieve shape propagation of a nucleating tauopathy fold. In this study, we ask whether jR2R3 P301L fibrils are active tau prions by showing recruitment of full-length intracellular tau over multiple passages and by achieving isoform-selective seeding. By introducing jR2R3 P301L fibrils into cells, we confirm the fibril, not the monomer, as the tau peptide that can template misfolding. Furthermore, the misfolding and induced conformational changes are seen in regions of tau well outside the 19-residue long jR2R3 segment, supporting our hypothesis that misfolding of a critical motif seeds the aggregation of many naive tau molecules and induces misfolding to the rest of the tau sequence. The so-treated intracellular tau forms sarkosyl insoluble material with properties that parallel human brain tauopathies, including MC1 antibody staining, fibril-like morphologies seen by TEM, and molecular weights that approximate these complex endogenous seed-competent assemblies.

Critical to the design of the jR2R3 P301L peptide is its correspondence to the R2R3 junction sequence, uniquely present in 4R tauopathy fibrils in AGD, PSP, CBD, ARTAG, GGT, and GPT (26), resulting in fibrils that require the precise 4R tau sequence to seed intracellular 4R tau. A 4R tau in which an amino acid substitution mimicked a 3R tau sequence could not be seeded. This shows that the location of templating that can differentiate between a 4R tau versus a 3R tau substrate must encompass the jR2R3 junction of the peptide we studied here. To observe such exquisite isoform selectivity between different tau constructs differing by a single residue at the jR2R3 junction, the orientation of hydrogen bond-forming backbone along the fibril axis is an insufficient condition. Rather, there must be a mechanism that aligns the tau monomer substrate on the surface of the tau fibril in which a hydrophobic hotspot, hyperlocalized around sites 300 and 301, pins the jR2R3 P301L peptide to the fibril end surface, in register.

The degree of ordering and selection extends beyond the region of tau corresponding to the peptide. The probability distribution of intramolecular distance(R) measured by DEER of jR2R3

P301L fibrils shows that at least two distinct structures form that are outside the core region identified by cryo-EM. The selection of only one of the peptide fibrils must be achieved to narrow the heterogeneity of the longer Tau187 fibrils seeded by the short jR2R3 peptide. As expected from the structure of the seed peptide, the DEER distances of seeded Tau187 fibrils were consistent with values expected from PSP or GPT. The selection of induced structures from the vast disordered landscape was more restricted than in heparin-induced fibrils (Fig. 5*A* and *SI Appendix*, Fig. S6*A*), but without the extraordinary fidelity of tau templating in the brain that generates one or very few tau structures.

The most salient feature of prion-like templating by jR2R3 P301L is its specificity for 4R tau. Such specificity must be rooted in a distinctive shape of the active fibril end that serves as a molecularly precise template and is thermodynamically capable of recruiting naive tau, with its PHF6 and its flanking domain in register to achieve templating. By substituting specific amino acids in the flanking sequence that will weaken or strengthen access to the PHF6 region, 4R tau can acquire or lose competence to initiate a 4R tauopathy fold. These substitutions are derived from those amino acids in jR1R3 that depart from jR2R3 and were inferred from the REMD. The simulations showed clear energetically accessible pathways from a shielded loop region due to H-bonding to a more accessible internal loop structure in jR2R3 that is prone to intermolecular H-bonds and hence oligomerization. The single amino acid substitution, S305K, that can prevent jR2R3-induced aggregation, suggested a site where a single codon substitution could prevent 4R tauopathies. As a point of background information, S305 is the last codon of MAPT exon 10, and is included in the RNA hairpin loop that regulates exon 10 alternative splicing. Although mutations have been identified in this codon that increase 4R tau, like all other splice site mutations, none of the mutations correspond to S305K used here for its effects on the tau protein (60). Interestingly, in vertebrate fish, the 305 position is commonly either a lysine or another polar residue such as arginine or asparagine (61).

Three factors potentially explain why the S305K mutation inhibits 4R tau aggregation: steric hindrance of the known 4R tau folds, increased hydration at the dewetting interface, and altered intramolecular H-bonding within monomers. Among four solved 4R tau folds, three—CBD, PSP, and GGT—have an S305 oriented inwardly within the strand-loop-strand motif (*SI Appendix*, Fig. S9). A bulky, inwardly pointing K305 side chain would sterically disrupt the side chain zipper, preventing these structures from forming. In contrast, a fourth 4R tau fold, termed "GPT," presents an S305 that faces outward from the strand-loop-strand motif, leaving this motif undisturbed by the bulky K305. However, even in this context, a K305 side chain would sterically disrupt contacts with I354 and L357 potentially impeding fibrillization. Besides steric considerations, the S305K mutation might disrupt aggregation due to its positively charged side chain which interacts favorably with water. Consequently, this side chain and the adjacent residues will be more resistant to dewetting, which is an essential step in nucleation and elongation. Recently, time-resolved cryoelectron microscopy detected a "first intermediate" on-pathway to Alzheimer and CTE fibrils consisting of an ordered core spanning residues 302 to 316 (62). Interestingly, the AD/CTE-precursor region includes the PHF6 region and C-terminal extension, but not the complete counter strand needed to form the SLS core of 4R tauopathy fibrils. This small shift relative to jR2R3 (295 to 313) may be enough for the region 302 to 316 to follow a different folding pathway and conformational rearrangement to ultimately generate fibrils resembling the 3R/4R tauopathy forms as observed in AD filaments.

Although the peptide here was derived from cryo-EM structures of tau, its relationship to in vivo proteoforms is unknown. Many small tau fragments have been reported in tauopathies; however, their role in disease is debated. The 19-amino acid sequence corresponds to a relatively "cleavage poor" region of tau (63) possibly related to the two histidines which is the only amino acid with a pKa within the physiological range and will make the peptide uniquely suited to be protonated inside the acidic lysosome. While mainly of interest as a heuristic probe, the resistance of the peptide to proteolysis under physiologic conditions may generate a similar peptide in vivo.

Many intracellular factors can lead to the nucleation and propagation of such tau peptides, as long as they contain amyloidogenic domains. The exposure to and compaction of the cellular space by lipid droplets or in some other entity may force the formation of hydrophobic bonds with an aqueous solvent and intermolecular hydrogen bonds found in tau aggregates. Solvent-exposed hydrophobic regions can favor interactions with low-molecular-weight hydrophobic or amphiphilic lipids known to interact with tau and induce aggregation (64). Within intrinsically disordered proteins, lipid binding occurs in more structured regions, such as the relatively more ordered repeat region in tau where its prion properties reside (65). Indeed, using solid-state NMR and transmission electron microscopy, a tau construct encoding the microtubule-binding repeats and a proline-rich domain was reconstituted into cholesterol-containing phospholipid membranes in a transition from a random coil to a β-sheet conformation over weeks (66). Cellular aggregates displayed colocalization with VCP and SQSTM1, proteins essential for aggresome formation and selective autophagy (49–51, 55, 67). SQSTM1, known to interact with tau and autophagosomes, has diminished expression in Alzheimer's disease (44), and its depletion leads to hyperphosphorylated tau accumulation (52). Meanwhile, VCP aids in the degradation of tau aggregates (51) and is crucial for proper aggresome formation (68), implicating a critical role for both proteins in the pathogenesis of tauopathies.

These studies suggest several entry points for 4R tauopathy interventions involving either nanobodies or small molecules, but all pointing to the junction spanning U-shape R2R3 structure with its relative exposure of the PHF6 amyloidogenic sequence capable of templating the fibril end surface. Structural studies suggest a similar rationale might be applied to the amyloid-beta-peptide (69). Furthermore, the dynamic size changes of the aggregates observed intracellularly may offer some potential for disaggregation approaches.

Materials and Methods

Preparation of Purified Tau Constructs. Peptides obtained from Genescript, all featuring uncapped termini, were dissolved in ddH_2O and stored immediately as 100 μM aliquots at −80 °C. The aggregation process was facilitated in a 50 mL Eppendorf tube where the stock peptide was reduced to a 50 μM concentration using 20 mM HEPES, pH 7.4, accompanied by a 4:1 ratio addition of 200 μM heparin (average molecular weight 16 kDa). Continuous shaking at 200 rpm in a 37 °C incubator was performed for 24 h. The resultant fibrils were isolated using a 50 kDa cutoff concentrator and rinsed three times with MilliQ water to remove excess heparin and monomeric peptide. The fibrils were then lyophilized overnight using a FreeZone 2.5 L −84 °C Benchtop Freeze Dryer. Upon quantification of the fibril mass, we reconstituted the seed stock to 1 mM using 20 mM HEPES, pH 7.4, and froze it at −80 °C. Tau187 expression and purification procedures followed previously reported methods. A detailed protocol is included in *SI Appendix, Methods*.

Cell Seeding Experiments. H4 neuroglioma cells stably expressing either mClover3-Tau187-WT, mClover3-Tau187-P301L, mClover3-0N4R-WT, mClover3-0N4R-P301L, mClover3-2N4R-WT, or mClover3-2N4R-P301L were cultured in DMEM, supplemented with 10% FBS, 100 μg/mL penicillin/streptomycin, and 500 μg/mL geneticin. The cell cultures were maintained in a humidified atmosphere of 5% CO_2 at 37 °C. For seeding experiments, cells were plated in 96-well

plates at a density of 20,000 cells per well. On the following day, cells were transfected with various tau species (at a final concentration of 2 μM unless stated otherwise) using 1.25 μL of Lipofectamine 2000 (Thermo Fisher) per well. The tau seeds were subjected to sonication for 30 s using the microtip of a Qsonica sonicator, operating at a 30% duty cycle. For the quantification of the assay, cells containing one or more puncta were counted and normalized by dividing by the total number of cells in each well. Each well in the cultured plate contributed one data point, and the quantification results were obtained from at least five independent cultures.

Fluorescence-guided O-PTIR imaging setup and spectral measurement. O-PTIR spectroscopy and coregistered fluorescence imaging were performed on a mIRage LS microscope (Photothermal Spectroscopy Corp.). Detailed parameters are included in *SI Appendix*, Methods. To prepare for O-PTIR spectroscopy measurements, the cells were rinsed twice with deionized water before drying in the air. For the data acquisition, we first acquired widefield fluorescence imaging to reveal the tau distribution in cells. We then pinned to puncta regions and puncta-free regions in cells to acquire O-PTIR spectra. The spectra spanned 1,480 to 1,800 cm^{-1} (5.55 to 6.75 μm), covering protein amide II, protein amide I, and lipids signal. Details of spectral analysis are included in *SI Appendix, Methods*.

Data, Materials, and Software Availability. All study data are included in the article and/or *SI Appendix*.

ACKNOWLEDGMENTS. We acknowledge support by the NIH grant 5R01AG056058-07 and the Rainwater Foundation. We acknowledge support from the Center for Scientific Computing at the California Nanosystems Institute (CNSI, NSF grant CNS-1725797) for the availability of high-performance computing resources and support. This work used the Extreme Science and Engineering Discovery Environment, which is supported by the NSF grant ACI-1548562 (MCA05S027). J.E.S. acknowledges support from the NSF (MCB-1716956). We acknowledge support from the W. M. Keck Foundation. We acknowledge the use of the NRI-MCDB Microscopy Facility and the Resonant Scanning Confocal supported by NSF MRI grant DBI-1625770.

Author affiliations: [a]Neuroscience Research Institute, University of California Santa Barbara, Santa Barbara, CA 93106; [b]Department of Molecular, Cell and Developmental Biology, University of California Santa Barbara, Santa Barbara, CA 93106; [c]Department of Chemistry and Biochemistry, University of California Santa Barbara, Santa Barbara, CA 93106; [d]Department of Chemical Engineering, University of California Santa Barbara, Santa Barbara, CA 93106; [e]Photothermal Spectroscopy Corp., Santa Barbara, CA 93101; [f]Center for Natural and Human Sciences, Federal University of ABC, São Bernardo do Campo, São Paulo 09600-000, Brazil; [g]University of Lille, Inserm, CHU Lille, Lille Neuroscience & Cognition Lille F-59000, France; [h]Laboratoire d'Excellence Development of Innovative Strategies for a Transdisciplinary Approach to Alzheimer's Disease, Alzheimer & Tauopathies Team, Lille F-59000, France; [i]Center National de la Recherche Scientifique Équipe de Recherche 9002–Integrative Structural Biology, Lille F-59000, France; [j]University of Lille, Inserm, Centre Hospitalier Universitaire de Lille, Institut Pasteur de Lille, U1167–Risk Factors and Molecular Determinants of Aging-Related Diseases Lille F-59000, France; and [k]Department of Physics, University of California Santa Barbara, Santa Barbara, CA 93106

1. V. M. Y. Lee, M. Goedert, J. Q. Trojanowski, Neurodegenerative tauopathies. *Annu. Rev. Neurosci.* **24**, 1121–1159 (2001).
2. M. Goedert, D. S. Eisenberg, R. A. Crowther, Propagation of Tau aggregates and neurodegeneration. *Annu. Rev. Neurosci.* **40**, 189–210 (2017).
3. N. Uemura, M. T. Uemura, K. C. Luk, V. M. Y. Lee, J. Q. Trojanowski, Cell-to-cell transmission of tau and α-synuclein. *Trends Mol. Med.* **26**, 936–952 (2020).
4. F. Clavaguera *et al.*, Transmission and spreading of tauopathy in transgenic mouse brain. *Nat. Cell Biol.* **11**, 909–913 (2009).
5. S. K. Kaufman, K. Del Tredici, T. L. Thomas, H. Braak, M. I. Diamond, Tau seeding activity begins in the transentorhinal/entorhinal regions and anticipates phospho-tau pathology in Alzheimer's disease and PART. *Acta Neuropathol.* **136**, 57–67 (2018).
6. S. L. DeVos *et al.*, Synaptic tau seeding precedes tau pathology in human Alzheimer's disease brain. *Front. Neurosci.* **12**, 267 (2018).
7. J. Vaquer-Alicea, M. I. Diamond, L. A. Joachimiak, Tau strains shape disease. *Acta Neuropathol.* **142**, 57–71 (2021).
8. S. S. Paul, A. Lyons, R. Kirchner, M. T. Woodside, Quantifying oligomer populations in real time during protein aggregation using single-molecule mass photometry. *ACS Nano* **16**, 16462–16470 (2022).
9. M. Kjaergaard *et al.*, Oligomer diversity during the aggregation of the repeat region of tau. *ACS Chem. Neurosci.* **9**, 3060–3071 (2009).
10. G. S. Bloom, Amyloid-β and Tau: The trigger and bullet in Alzheimer disease pathogenesis. *JAMA Neurol.* **71**, 505–508 (2014).
11. A. Šarić, T. C. T. Michaels, A. Zaccone, T. P. J. Knowles, D. Frenkel, Kinetics of spontaneous filament nucleation via oligomers: Insights from theory and simulation. *J. Chem. Phys.* **145**, 211926 (2016).
12. M. P. Vigers *et al.*, Tau P301L mutation promotes core 4R tauopathy fibril fold through near-surface water structuring and conformational rearrangement. bioRxiv [Preprint] (2023). https://doi.org/10.1101/2023.11.28.568818 (Accessed 28 November 2023).
13. P. Ganguly *et al.*, Tau assembly: The dominant role of PHF6 (VQIVYK) in microtubule binding region repeat R3. *J. Phys. Chem. B* **119**, 4582–4593 (2015).
14. W. J. Goux *et al.*, The formation of straight and twisted filaments from short tau peptides. *J. Biol. Chem.* **279**, 26868–26875 (2004).
15. C. Fagnen, J. Giovannini, M. Catto, A. S. Voisin-Chiret, J. Sopkova-de Oliveira Santos, On the tracks of the aggregation mechanism of the PHF6 peptide from tau protein: Molecular dynamics, energy, and interaction network investigations. *ACS Chem. Neurosci.* **13**, 2874–2887 (2022).
16. P. M. Seidler *et al.*, Structure-based inhibitors of tau aggregation. *Nat. Chem* **10**, 170–176 (2018).
17. T. Altendorf *et al.*, Stabilization of monomeric tau protein by all D-enantiomeric peptide ligands as therapeutic strategy for Alzheimer's disease and other tauopathies. *Int. J. Mol. Sci.* **24**, 2161 (2023).
18. I. Aillaud, S. A. Funke, Tau aggregation inhibiting peptides as potential therapeutics for Alzheimer disease. *Cell Mol. Neurobiol.* **43**, 951–961 (2023).
19. C. Danis *et al.*, Inhibition of Tau seeding by targeting Tau nucleation core within neurons with a single domain antibody fragment. *Mol. Ther.* **30**, 1484–1499 (2022).
20. S. A. Mok *et al.*, Mapping interactions with the chaperone network reveals factors that protect against tau aggregation. *Nat. Struct. Mol. Biol.* **25**, 384–393 (2018).
21. H. Mirbaha, B. B. Holmes, D. W. Sanders, J. Bieschke, M. I. Diamond, Tau trimers are the minimal propagation unit spontaneously internalized to seed intracellular aggregation. *J. Biol. Chem.* **290**, 14893–14903 (2015).
22. N. Annadurai, L. Malina, J. Malohlava, M. Hajdúch, V. Das, Tau R2 and R3 are essential regions for tau aggregation, seeding and propagation. *Biochim.* **200**, 79–86 (2022).
23. H. Mirbaha *et al.*, Seed-competent tau monomer initiates pathology in a tauopathy mouse model. *J. Biol. Chem.* **298**, 102163 (2022).
24. D. Chen *et al.*, Tau local structure shields an amyloid-forming motif and controls aggregation propensity. *Nat. Commun.* **10**, 2493 (2019).
25. J. Stöhr *et al.*, A 31-residue peptide induces aggregation of tau's microtubule-binding region in cells. *Nat. Chem.* **9**, 874–881 (2017).
26. T. Arai *et al.*, Distinct isoforms of tau aggregated in neurons and glial cells in brains of patients with Pick's disease, corticobasal degeneration and progressive supranuclear palsy. *Acta Neuropathol.* **101**, 167–173 (2001).
27. S. Podvin *et al.*, Dysregulation of neuropeptide and tau peptide signatures in human Alzheimer's disease brain. *ACS Chem. Neurosci.* **13**, 1992–2005 (2022).
28. C. Sato *et al.*, Tau kinetics in neurons and the human central nervous system. *Neuron* **97**, 1284–1298.e7 (2018).
29. P. Bros *et al.*, Antibody-free quantification of seven tau peptides in human CSF using targeted mass spectrometry. *Front. Neurosci.* **9**, 302 (2015).
30. S. H. Scheres, W. Zhang, B. Falcon, M. Goedert, Cryo-EM structures of tau filaments. *Curr. Opin. Struct. Biol.* **64**, 17–25 (2020).
31. W. Zhang *et al.*, Novel tau filament fold in corticobasal degeneration. *Nature* **580**, 283–287 (2020).
32. A. W. P. Fitzpatrick *et al.*, Cryo-EM structures of tau filaments from Alzheimer's disease. *Nature* **547**, 185–190 (2017).
33. W. Zhang *et al.*, Heparin-induced tau filaments are polymorphic and differ from those in Alzheimer's and Pick's diseases. *ELife* **8**, e43584 (2019).
34. Y. Shi *et al.*, Structure-based classification of tauopathies. *Nature* **598**, 359–363 (2021).
35. B. Falcon *et al.*, Structures of filaments from Pick's disease reveal a novel tau protein fold. *Nature* **561**, 137–140 (2018).
36. A. J. Dregni *et al.*, Fluent molecular mixing of tau isoforms in Alzheimer's disease neurofibrillary tangles. *Nat. Commun.* **13**, 2967 (2022).
37. B. Combs, N. M. Kanaan, Exposure of the amino terminus of tau is a pathological event in multiple tauopathies. *Am. J. Pathol.* **187**, 1222–1229 (2017).
38. A. Tarutani *et al.*, Human tauopathy-derived tau strains determine the substrates recruited for templated amplification. *Brain* **144**, 2333–2348 (2021).
39. T. Maiuri *et al.*, Huntingtin is a scaffolding protein in the ATM oxidative DNA damage response complex. *Hum. Mol. Genet.* **26**, 395–406 (2017).
40. Y. Bai, J. Yin, J.-X. Cheng, Bond-selective imaging by optically sensing the mid-infrared photothermal effect. *Sci. Adv.* **7**, eabg1559 (2021).
41. I. M. Pavlovetc *et al.*, Infrared photothermal heterodyne imaging: Contrast mechanism and detection limits. *J. Appl. Phys.* **127**, 165101 (2020).
42. Q. Xia, J. Yin, Z. Guo, J.-X. Cheng, Mid-infrared photothermal microscopy: Principle, instrumentation, and applications. *J. Phys. Chem. B* **126**, 8597–8613 (2022).
43. C. Prater *et al.*, Fluorescently guided optical photothermal infrared microspectroscopy for protein-specific bioimaging at subcellular level. *J. Med. Chem.* **66**, 2542–2549 (2023).
44. N. V. Gorantla, S. Chinnathambi, Autophagic pathways to clear the tau aggregates in Alzheimer's disease. *Cell Mol. Neurobiol.* **41**, 1175–1181 (2021).
45. M. A. Rahman *et al.*, Autophagy modulation in aggresome formation: Emerging implications and treatments of Alzheimer's disease. *Biomedicines* **10**, 1027 (2022).
46. J. M. T. Hyttinen *et al.*, Clearance of misfolded and aggregated proteins by aggrephagy and implications for aggregation diseases. *Ageing Res. Rev.* **18**, 16–28 (2014).
47. K. Zatloukal *et al.*, p62 is a common component of cytoplasmic inclusions in protein aggregation diseases. *Am. J. Pathol.* **160**, 255–263 (2002).
48. D. C. Carrettiero *et al.*, Stress routes clients to the proteasome via a BAG2 ubiquitin-independent degradation condensate. *Nat. Commun.* **13**, 3074 (2022).
49. P. Sánchez-Martín, M. Komatsu, p62/SQSTM1–Steering the cell through health and disease. *J. Cell Sci.* **131**, jcs222836 (2018).

50. J. R. Babu, T. Geetha, M. W. Wooten, Sequestosome 1/p62 shuttles polyubiquitinated tau for proteasomal degradation. *J. Neurochem.* **94**, 192–203 (2005).
51. I. Saha *et al.*, The AAA+ chaperone VCP disaggregates Tau fibrils and generates aggregate seeds in a cellular system. *Nat. Commun.* **14**, 560 (2023).
52. J. Ramesh Babu *et al.*, Genetic inactivation of p62 leads to accumulation of hyperphosphorylated tau and neurodegeneration. *J. Neurochem.* **106**, 107–120 (2008).
53. F. X. Blaudin de Thé *et al.*, P62 accumulates through neuroanatomical circuits in response to tauopathy propagation. *Acta Neuropathol. Commun.* **9**, 177 (2021).
54. J. F. Abisambra *et al.*, Tau accumulation activates the unfolded protein response by impairing endoplasmic reticulum-associated degradation. *J. Neurosci.* **33**, 9498–9507 (2013).
55. Y. Xu, S. Zhang, H. Zheng, The cargo receptor SQSTM1 ameliorates neurofibrillary tangle pathology and spreading through selective targeting of pathological MAPT (microtubule associated protein tau). *Autophagy* **15**, 583–598 (2019).
56. E. Dimou *et al.*, Super-resolution imaging unveils the self-replication of tau aggregates upon seeding. *Cell Rep.* **42**, 112725 (2023).
57. M. R. Sawaya *et al.*, Atomic structures of amyloid cross-β spines reveal varied steric zippers. *Nature* **447**, 453–457 (2007).
58. L. Wu, S. S. Madhavan, C. Tan, B. Xu, Hexameric aggregation nucleation core sequences and diversity of pathogenic tau strains. *Pathogens* **11**, 1559 (2022).
59. L. Larini *et al.*, Initiation of assembly of tau(273–284) and its ΔK280 mutant: An experimental and computational study. *Phys. Chem. Chem. Phys.* **15**, 8916–8928 (2013).
60. M. Iijima *et al.*, A distinct familial presenile dementia with a novel missense mutation in the tau gene. *NeuroReport* **10**, 497 (1999).
61. N. I. Trushina, L. Bakota, A. Y. Mulkidjanian, R. Brandt, The evolution of tau phosphorylation and interactions. *Front. Aging Neurosci.* **11**, 256 (2019).
62. S. Lövestam *et al.*, Disease-specific tau filaments assemble via polymorphic intermediates. *Nature* **625**, 119–125 (2024).
63. P. J. Sampognaro *et al.*, Mutations in α-synuclein, TDP-43 and tau prolong protein half-life through diminished degradation by lysosomal proteases. *Mol. Neurodegener.* **18**, 29 (2023).
64. M. E. King, T. C. Gamblin, J. Kuret, L. I. Binder, Differential assembly of human tau isoforms in the presence of arachidonic acid. *J. Neurochem.* **74**, 1749–1757 (2000).
65. E. Deryusheva *et al.*, Does intrinsic disorder in proteins favor their interaction with lipids? *Proteomics* **19**, 1800098 (2019).
66. N. El Mammeri, O. Gampp, P. Duan, M. Hong, Membrane-induced tau amyloid fibrils. *Commun. Biol.* **6**, 467 (2023).
67. M. Ono *et al.*, Central role for p62/SQSTM1 in the elimination of toxic tau species in a mouse model of tauopathy. *Aging Cell* **21**, e13615 (2022).
68. S. Mukkavalli, J. A. Klickstein, B. Ortiz, P. Juo, M. Raman, The p97–UBXN1 complex regulates aggresome formation. *J. Cell Sci.* **134**, jcs254201 (2021).
69. M. Khaled *et al.*, A hairpin motif in the amyloid-β peptide is important for formation of disease-related oligomers. *J. Am. Chem. Soc.* **145**, 18340–18354 (2023).